Bioactive Materials 5 (2020) 348–357

Contents lists available at ScienceDirect

Bioactive Materials

journal homepage: http://www.keaipublishing.com/biomat

Enhanced osteogenesis and therapy of osteoporosis using simvastatin loaded hybrid system

Tao Wu[a,1], Jing Sun[a,1], Lei Tan[b], Qi Yan[a], Lei Li[a], Liangwen Chen[a], Xiangmei Liu[b,*], Shi Bin[a,**]

[a] The State Key Laboratory Breeding Base of Basic Science of Stomatology (Hubei-MOST) & Key Laboratory of Oral Biomedicine Ministry of Education, Department of Dental Implantology, School & Hospital of Stomatology, Wuhan University, 237 Luoyu Road, Wuhan, 430079, PR China

[b] Ministry-of-Education Key Laboratory for the Green Preparation and Application of Functional Materials, Hubei Key Laboratory of Polymer Materials, School of Materials Science & Engineering, Hubei University, Wuhan, 430062, China

ARTICLE INFO

Keywords:
Osteogenesis
Osteoporosis
Mesoporous hydroxyapatite
Bone marrow stromal cells
Drug release

ABSTRACT

Postmenopausal osteoporosis is a common chronic dynamic bone disorder, caused by estrogen deficiency. To address this issue, we constructed a controlled drug-release system composed of poly (N-isopropylacrylamide) brush modified mesoporous hydroxyapatite (MHA-SIM-P) loaded with simvastatin (SIM) using an ovariectomised (OVX) rat model. Quantitative alkaline phosphatase activity assay, alizarin red staining and RT-PCR were tested to evaluate the osteogenic ability *in vitro*. The results showed that the MHA-SIM-P nanoparticles significantly improved the osteogenic differentiation of OVX bone marrow stromal cells (BMSCs) *in vitro*. In osteoporotic animal model, the therapeutic efficiency for bone defect was evaluated by μCT analysis, tartrate-resistant acid phosphatase, haematoxylin and eosin staining, which showed improved bone formation and less osteoclastic response in OVX rats after surgery for 3 and 6 weeks. This polymer brush modified MHA system provided a sustained release system of hydrophobic SIM to inhibit osteoporosis together with MHA nanoparticle promoting the osteogenesis. Thus, this novel strategy exhibited great potential for promoting osteogenic ability and treating local osteoporotic defects.

1. Introduction

Postmenopausal osteoporosis is a common chronic dynamic bone disorder, caused by hormone changes with age which damage osteoblast function and increase osteoclastic activity [1–4]. Osteoporosis is a worldwide challenge impacting millions of people, with female being significantly more affected than males [5]. For people with osteoporosis, bone fracture are more common, and the ability to self-heal is hampered [6]. Approaches to treat osteoporosis are mainly focused on suppressing bone resorption, through the use of biophosphonates, calcitonin, oestrogens, and selective oestrogen receptor modulators; or through promoting bone formation, such as fluoride, and PTH. However, the systemic treatment of osteoporosis with the aforementioned approaches always causes some side effects [7]. On the contrary, local controlled drug release treatment provides a new method of treating osteoporosis without side effects, especially osteoporotic bone defects [8].

The use of autografts is the golden standard method of repairing bone defects. Hydroxyapatite (HA), which comprises 60–70% of the bone matrix, had been regarded as one of the most extensively used artificial bone substitutes due to its excellent biocompatibility [9–12]. Mesoporous hydroxyapatite (MHA) is the mesoporous condition of HA. MHA possesses controlled pore size, well-organised pores and optimised pore volume [13–15]. Therefore, it can be an effective drug carrier to realise drug delivery [16,17]. Recently, a greater focus has been placed on the modification of MHA to make it a controlled drug release system. As for the modification method, Poly(N-isopropylacrylamide) is a thermal-responsive polymer. Below 32 °C, its polymer chains have demonstrated anextended conformation in water to load drugs into the mesopores, and above 32 °C, collapse on the surface of mesoporous particles in a hydrophobic state to achieve long-term hydrophobic drug release (Fig. 1a) [18]. When MHA and Poly(N-isopropylacrylamide) are combined, a drug releasing system is well established and drugs can be stored in the mesopores of MHA particles.

Peer review under responsibility of KeAi Communications Co., Ltd.

* Corresponding author.
** Corresponding author.
E-mail addresses: liuxinagmei1978@163.com (X. Liu), shibin_dentist@whu.edu.cn (S. Bin).

[1] These authors contributed equally to this work.

https://doi.org/10.1016/j.bioactmat.2020.03.004
Received 7 February 2020; Received in revised form 1 March 2020; Accepted 6 March 2020

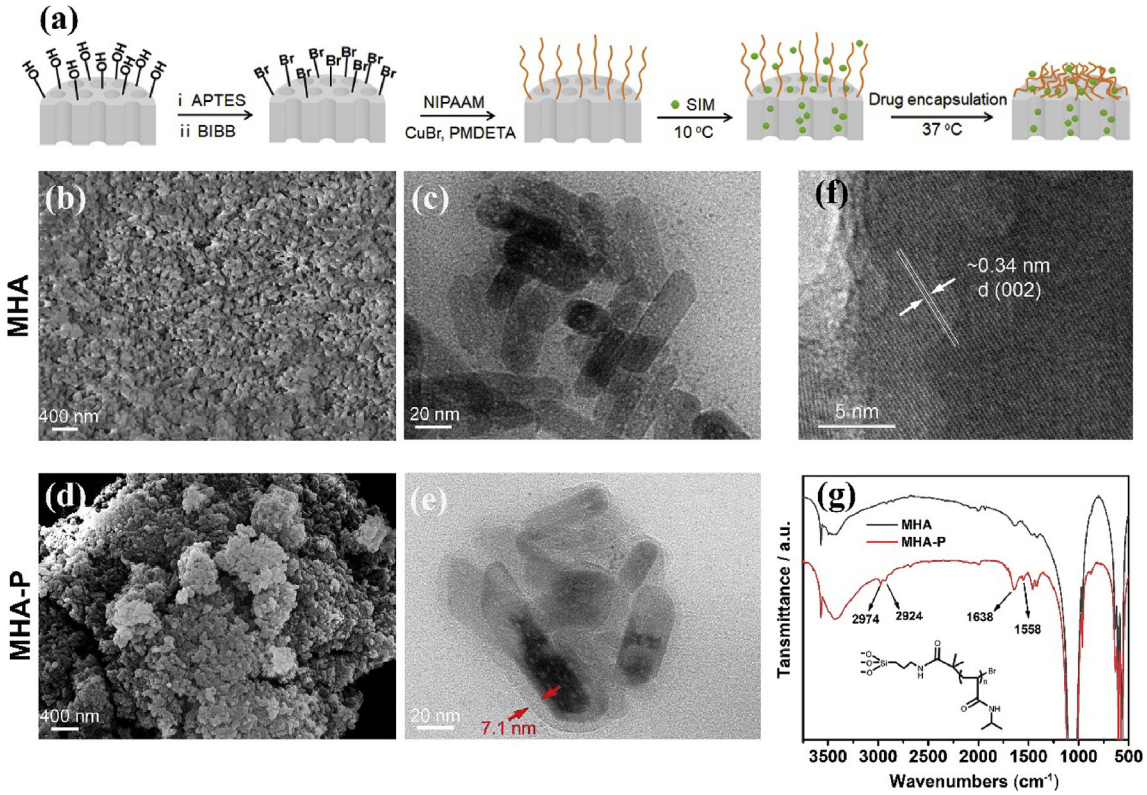

Fig. 1. Fabrication process illustration of MHA-SIM-P (a). SEM (b,d) and TEM (c,e) images of MHA an MHA-P. HRTEM image of MHA (f). FT-IR spectrometer of MHA and MHA-P (g).

Simvastatin (SIM), widely used in the treatment of hyperlipidaemia, has recently been administered as a bone growth medicine. The melting point of SIM is 139 °C, and its physical property is relative stable [19]. SIM may effectively treat bone defects in osteoporosis. The SIM molecular mechanism functions on bone repair can be concluded as up-regulating (such as BMP-Smad signalling pathway and VEGF signalling pathway) or down-regulating (such as TNF-α-to-Ras/Rho/MAPK pathway and the phosphatidylinositide-3 kinase pathway) several signal pathways [20,21]. Due to the possible effects of SIM on bone defects, we have tried to understand the effects of SIM on bone defects from osteoporosis, to verify whether SIM can strengthen the bone's healing ability. However, the SIM is hard to release sustainably and locally *in vivo* due to its hydrophobic property.

Considering the hydrophobicity of SIM, poly (N-isopropylacrylamide) brush modified mesoporous hydroxyapatite (MHA-SIM-P) was fabricated *via* a surface-initiated atom transfer radical polymerisation (SI-ATRP) method, which controlled the sustained release of the hydrophobic SIM. This study aimed to evaluate the osteogenic ability of MHA-SIM-P nanoparticles on BMSCs derived from ovariectomised (OVX) rats and the repair of femur defects.

2. Materials and method

2.1. Materials

FITC-phalloidin, dexamethasone, 3-isobutyl-1-methylxanthine, insulin, L-ascorbic acid, indomethacin, sodium pyruvate, β-glycerol phosphate, TGF-β and a tartrate-resistant acid phosphatase (TRAP) staining kit were bought from Sigma-Aldrich. α-MEM, foetal bovine serum (FBS) and penicillin/streptomycin (P/S) solution were bought from HyClone. SIM was bought from Calbiochem®. Triton X-100 and Alcian blue power were bought from Amresco. ITS + Premix, CD 45 and CD90 antibodies were purchased from BD Biosciences. N-isopropylacrylamide, 2-Bromoisobutyryl bromide (BIBB) and N,N,N′,N′,N"-pentamethyldiethylenetriamine, Alizarin Red power, Oil Red power were purchased from Aladdin.

2.2. Animals and surgical protocols

Animal surgical procedures were performed based on the guidelines for animal care and use as set forth by the Wuhan University committee, People's Republic of China, and approved by the Ethics Committee at the School of Dentistry. All operations were carried out in sterile conditions in the specific pathogen free (SPF) level animal centre. Postoperative penicillium (40000 IU/mL) was administrated intramuscularly for 3 days.

2.2.1. Osteoporotic model

After anesthetisation (chloral hydrate, 4 mL/kg body weight), 8-week-old Wistar rats underwent a bilateral ovariectomy. A vertical incision was made between the femur on the stomach, and the ovary was blunt dissected and ligated. Then the muscles and skin were repositioned layer-by-layer and sutured.

2.2.2. Femur defect model

Two months after the OVX surgery, rats were divided into 4 groups (n = 5 per group) randomly: (1) Sham; (2) Blank; (3) MHA; (4) MHA-SIM-P. A 1 cm-length incision in the distal femoral was made and the muscles were blunt dissected on both sides. Next, a 2.5 mm-diameter bicortical defect was drilled beneath the growth plate by using a trephine bur at a speed of 700 rpm and saline solution irrigation was administered. Saline solution was injected to remove bone debris. MHA-SIM-P or MHA nanoparticles were filled the drilled defects. The rats were sacrificed at 3 or 6 weeks randomly following femur drilling and specimens were collected for evaluation at a later date.

2.3. BMSCs isolation and in vitro culture

Two months later after the OVX surgery, OVX and Sham BMSCs were harvested. After the rats had been euthanised, cervical dislocation was executed and marrow fluids were eluted from the femur and tibia by α-MEM. Next, 15% foetal bovine serum and 1% penicillin/streptomycin solution was added to the cell medium. The isolated BMSCs were cultured in a 5% CO_2 incubator at 37 ˚C. Cells were used in the following study after two passages [22,23].

2.4. Preparation of MHA-SIM-P

K_2HPO_4 (2.7 g) and CTAB (4.3 g) were dissolved in DI H_2O (60 mL). Subsequently, NaOH (1.1 M, 15 mL) was added to regulate the pH to 12.0. Next, $CaCl_2$ (0.4 M, 30 mL) was mixed and stirred at 120 ˚C for 1 day. The sediment was purified by DI H_2O, and was sintered at 600 ˚C for 5 h before use. The prepared MHA (1.0 g) and 1 mL 3-aminopropyl triethoxysilane (APTES) were dispersed into 20 mL anhydrous toluene *via* ultrasonic dispersion. The dispersion was fully stirred under reflux for 1 day. The amino modified MHA was purified with toluene and ethanol thoroughly to remove unreacted APTES, and finally vacuum dried at 80 ˚C overnight. The prepared MHA-NH_2 (0.8 g) and anhydrous triethylamine (0.7 mL) were mixed with cold anhydrous dichloromethane and stirred. Next, BIBB (0.7 mL) was added into the above dispersion and stirred for 1.5 h under an ice-bath, then stirred at room temperature for another 24 h. The MHA-Br was purified by dichloromethane, deionised water and ethanol, respectively, and vacuum dried. The MHA-Br (95.0 mg), N-isopropylacrylamide (0.5 g) and PMDETA (32 μL) were dispersed in deionised water/methanol (1:1, 4 mL) and placed in a polymerisation pipe. The pipe was treated with two cycles of two freeze-pump-thaw under Ar gas to remove the air in the pipe. Subsequently, CuBr (7.5 mg) was put into the pipe and the pipe was operated as above for two cycles, and reacted at 27 ˚C for 1 day to get MHA-P. The MHA-P were purified by dimethyl formamide and deionised water, respectively, and vacuum dried at 60 ˚C overnight. MHA-P (130.0 mg) was dispersed in 5 mL DI H_2O through ultrasonic dispersion under an ice-bath. Next, the SIM dissolved in the ethanol solution (5 mL, 0.5 mM) was added into the dispersion of MHA-P solution and stirred for 1 day. Finally, the solvent was removed by rotary evaporation and the final MHA-SIM-P power was obtained through vacuum drying (Fig. 1a).

2.5. Preparation of SIM dissolution extracts

After sterilisation, the MHA-SIM-P (10 mg) was placed in the culture medium of α-MEM to remove unloaded SIM for 24 h at 20 ˚C. Then, every 10 mg nanoparticles were soaked in a culture medium (40 mL) at 37 ˚C for 24 h. It was then centrifuged at 1000 rpm for 1 min and filtrated before the following experiments.

2.6. Fluorescence microscopy analysis

Cell slides were prepared in advance and 1×10^4 OVX or Sham BMSCs per well were seeded on 24-well and cultured for 3 days. Next, the cells on the slides were fixed with 4% paraformaldehyde. FITC-phalloidin (5 μg/mL) was applied to incubated cells for 1 h. After they were washed two more times, DAPI (10 μg/mL) was used to stain the nucleus for 5 min. The photos were recorded through a fluorescent microscopy (Cannon, Japan).

2.7. Alkaline phosphatase (ALP) activity

OVX BMSCs were cultured in a culture medium for 24 h and the culture medium was replaced with an osteogenic material dissolution. The ALP activity of OVX BMSCs was tested after 7 or 14 days. Samples were treated with 150 μL per well of 0.3% Triton X-100 to dissolve the cells, and cell suspensions were collected and centrifuged at 14000 rcf for 10 min at 4 ˚C. Next, ALP activity and total protein content of cell lysates were detected by and BCA kit (Beyotime, China), respectively [24].

2.8. Alizarin red staining

OVX BMSCs culture condition was conducted as above. 1% Alizarin Red solution was prepared and the pH was adjusted to 4.2. At 14 days, cells were fixed and stained by Alizarin Red for 15 min and washed with DI H_2O. The stained mineralised nodule was photographed using a digital camera (Cannon, Japan).

2.9. Quantitative RT-PCR analysis

Total RNA was isolated by Trizol reagent (Invitrogen, Carsbad, USA), and a reverse transcription Takara kit (Takara, Japan) was used to form cDNAs. Quantitative RT-PCR was performed with an Applied Biosystem using SYBR Green (Takara, Japan). The protocol was as follows: denaturation at 95 ˚C for 10 min, amplification at 95 ˚C for 15 s, and anneal and links extension at 60 ˚C for 1 min. The primer sequences are as follows: *Runx2* F: ATCCAGCCACCTTCACTTACACC, R: GGGACCATTGGGAACTGATAGG; *OCN* F: CTGAACAAAGCCTTCATGT CCA, R: CACATACCCTAAACGGTGGT; *Gapdh* F: ACCACAGTCCATGCC ATCAC, R: TCCACCACCCTGTTGCTGTA.

2.10. Micro-computerized tomography (μCT) analysis of femoral defect regeneration

All femurs were fixed with 4% parafomadelyde for 48 h and scanned by μCT (CT50, Scanco Medical, Basersdorf, Switzerland). Scanning tooke placeat 70 kV and 114 μA with a thickness of 24 μm per slice to evaluate the new bone formation. All samples were fixed in EP tubes and placed in a cylindrical holder to ensure they were perpendicular to the X-ray beam (Fig. 3). Bone volume over total volume (BV/TV), the mean trabecular number (TB. N), and the mean trabecular separation (Tb. Sp) were evaluated.

2.11. Histological and immunohistochemical analysis

The obtained tissues were decalcified with 10% ethylene diamine tetraacetic acid (EDTA) for 8 weeks. The tissues were routinely dehydrated, embedded and cut into 4 μm sections. Haematoxylin and eosin (H&E) staining and Tartrate-resistant acid phosphatase (TRAP) staining were conducted. Immunohistochemical staining was performed to measure the expression of osteogenic genes including osteopontin (OPN) and bone sialo protein (BSP). For the immunohistochemical assessment, the primary anti-OPN (1:100) and anti-BSP (1:100) were used in a humidified chamber at 4 ˚C overnight. Next, sections were treated with a biotinylated secondary antibody (Beyotime, China) for 20 min before being incubated with a horseradish peroxidase-conjugated avidin-biotin complex (ABC) for another 20 min, followed by being buffered at 3,3-diaminobenzidiinetetrahydrochloride (DAB).

3. Results

3.1. Characterisations of MHA-P

The scanning electron microscope (SEM) (QUANTA 200, The Netherlands) images of the samples (Fig. 1b,d) presented the uniformly distributed nanostructure particles for both MHA and MHA-P. The transmission electron microscope (TEM) (HRTEM, JEOL, JEM-2010FEF, Japan) images showed that these nanoparticles were rod-like with ~4 nm pores. A 7.1 nm organic layer was covering the MHA-P, suggesting the existence of polymer on the MHA surface (Fig. 1c,e). As shown in Fig. 1f, the high-resolution TEM (HRTEM) image showed that

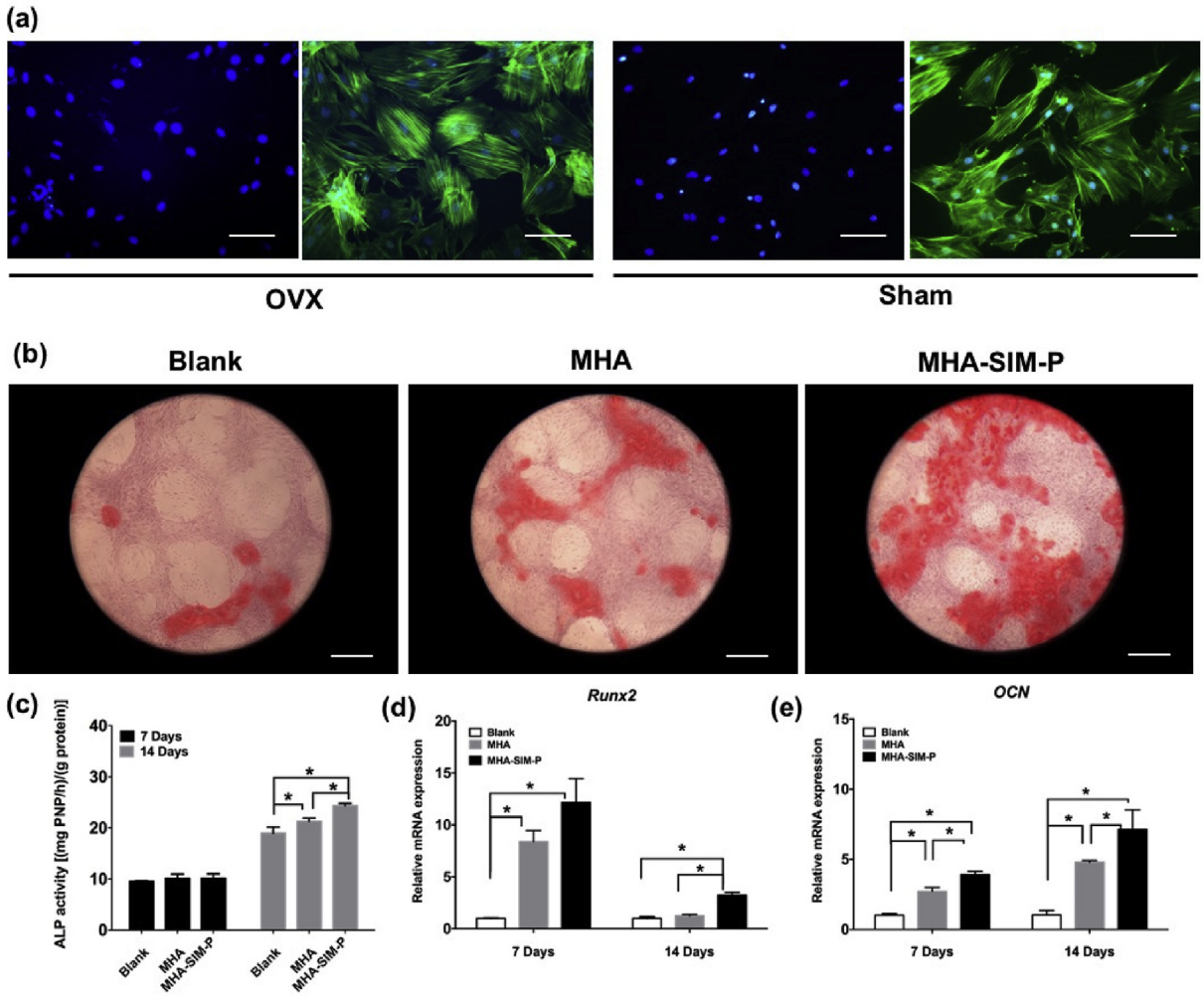

Fig. 2. Fluorescence microscopy images of the cellular skeleton of OVX and sham BMSCs (a; bar = 100 μm). Alizarin Red staining of OVX BMSCs among Blank, MHA, or MHA-SIM-P in osteogenic medium for 14 days (b; bar = 200 μm). Quantitative ALP activity of OVX BMSCs cultured in Blank, MHA, and MHA-SIM-P in osteogenic medium extracts for 7 and 14 days (c). mRNA expression of *Runx2* (d) and *OCN* (e) in OVX BMSCs after osteogenic differentiation for 7 or 14 days. n = 3 per group; *p < 0.05.

the lattice spacing with 0.34 nm attributed to the (002) plane lattice of MHA, demonstrating its typical hexagonal structure [25]. The fourier transform infrared spectrometer (FT-IR) (Nicolet IS10, USA) results shown in Fig. 1g showed that in contrast to MHA, the arisen peaks of the amide group at 1558 cm^{-1} and the $–CH_2$ group at 2974 and 2924 cm^{-1} from MHA-P prove that the Poly(N-isopropylacrylamide) had successfully grafted onto MHA. Since the SIM loading process in this experiment was at operated under an ice-bath and there is no functional group in MHA-P can react with SIM. So, the SIM is stable during the preparation of MHA-SIM-P.

3.2. Cell morphology of OVX and Sham BMSCs

The morphology of OVX and Sham BMSCs were observed by staining the actin filaments under fluorescence microscopy. The cellular skeleton of OVX and Sham BMSCs were clear stained after 7 days of incubation. OVX BMSCs showed polygonal, short and fat shape, while Sham BMSCs were slender and shaped like a spindle. No typical differences were exhibited in cell nuclei between OVX and Sham BMSCs (Fig. 2a).

3.3. Osteogenic differentiation of OVX BMSCs

To test the osteogenic ability of MHA-SIM-P on OVX BMSCs, Alizarin Red staining was conducted in the osteogenic material dissolution after 14 days. The amount of mineralisation nodule in the MHA-SIM-P group presented the largest, while the matrix deposition in the MHA group exhibited better than the Blank group (Fig. 2b).

The ALP activity of the OVX BMSCs was tested after the treatment of the osteogenic material dissolution (Fig. 2c). No statistical difference was observed in OVX BMSCs after 7 days of culturing. However, ALP activity in the MHA-SIM-P group represented the best performance, while the Blank group represented the lowest statistical performance. As a result of the above ALP activity, it appears that both MHA-SIM-P and MHA can enhance ALP activity, but that MHA-SIM-P's performance is better.

To further gain an insight into the role of MHA-SIM-P in osteoblastic differentiation, OVX BMSCs were examined after induction for 7 and 14 days for mRNA levels of *Runx2* and *OCN* expression (Fig. 2d and e). The total *Runx2* mRNA expression was decreased following the culturing time. A significant increase was detected in the MHA and MHA-SIM-P group at day 7, but at day 14, only the MHA-SIM-P group displayed a remarkably increased *Runx2* mRNA expression as compared to the other two groups (Fig. 2d). The *OCN* mRNA levels of the MHA-SIM-P group revealed more than the other two groups at day 7, and an increasing trend was demonstrated with a range of MHA-SIM-P > MHA > Blank at day 14 (Fig. 2e).

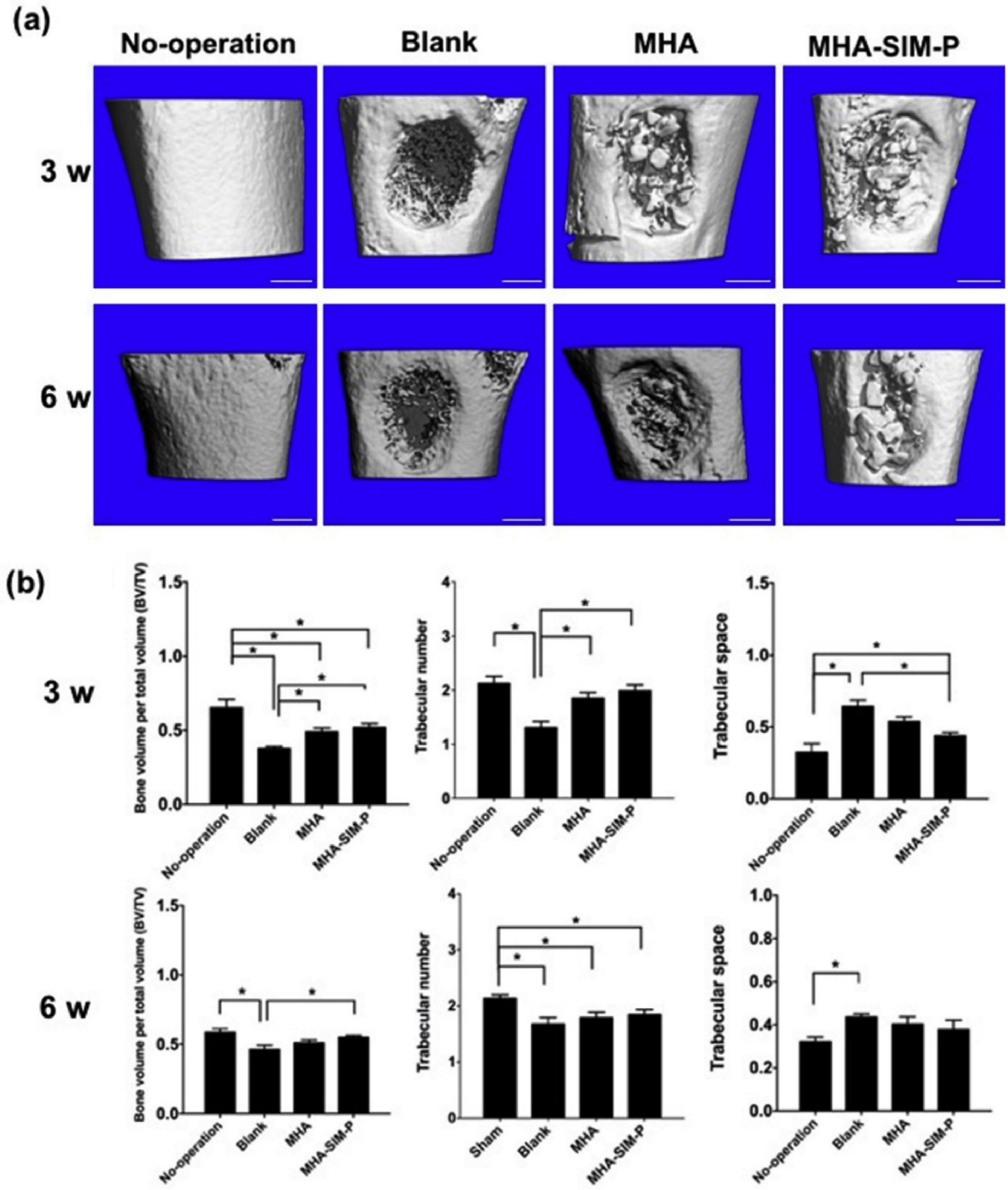

Fig. 3. 3D-μCT images of mineralised bone formation among No-operation, Blank, MHA, and MHA-SIM-P groups in OVX rats at 3 and 6 weeks (a; bar = 1 mm). Quantitative data of BV/TV, and Tb.N, and Tb.Sp within defects among No-operation, Blank, MHA, and MHA-SIM-P groups in rats at 3 and 6 weeks (b). n = 3 per group; *p < 0.05.

3.4. μCT analysis of femoral defect regeneration

As shown in Fig. 3a, the 3D μCT images of femur bone defect showed that the greatest amount of new bone formation was observed in the MHA-SIM-P group after surgery for 3 or 6 weeks. Parameters of BV/TV, trabecular number (Tb. N) and trabecular space (Tb. Sp) were taken to analyse the mineralised bone tissue for defects (Fig. 3b). In the Blank group, BV/TV (37.7%) at 3 weeks was relatively lower than BV/TV (46.3%) at 6 weeks, and Tb.Sp (0.643 mm) at 3 weeks was wider than Tb.Sp (0.436 mm) at 6 weeks, demonstrating sparsely new bone formation without treatment. At 3 weeks, MHA-SIM-P and MHA nanoparticles showed a similar increase trend in BV/TV and Tb. N as compared to the Blank group. A significant decrease in Tb. Sp (0.438 mm) of MHA-SIM-P was observed compared to the Blank group. At 6 weeks, BV/TV (55.1%) in the MHA-SIM-P group was superior to that of the Blank group. However, no differences were exhibited in BV/TV between MHA and the Blank group at 6 weeks, and statistical difference of Tb. N was only noticed in the no-operation group as

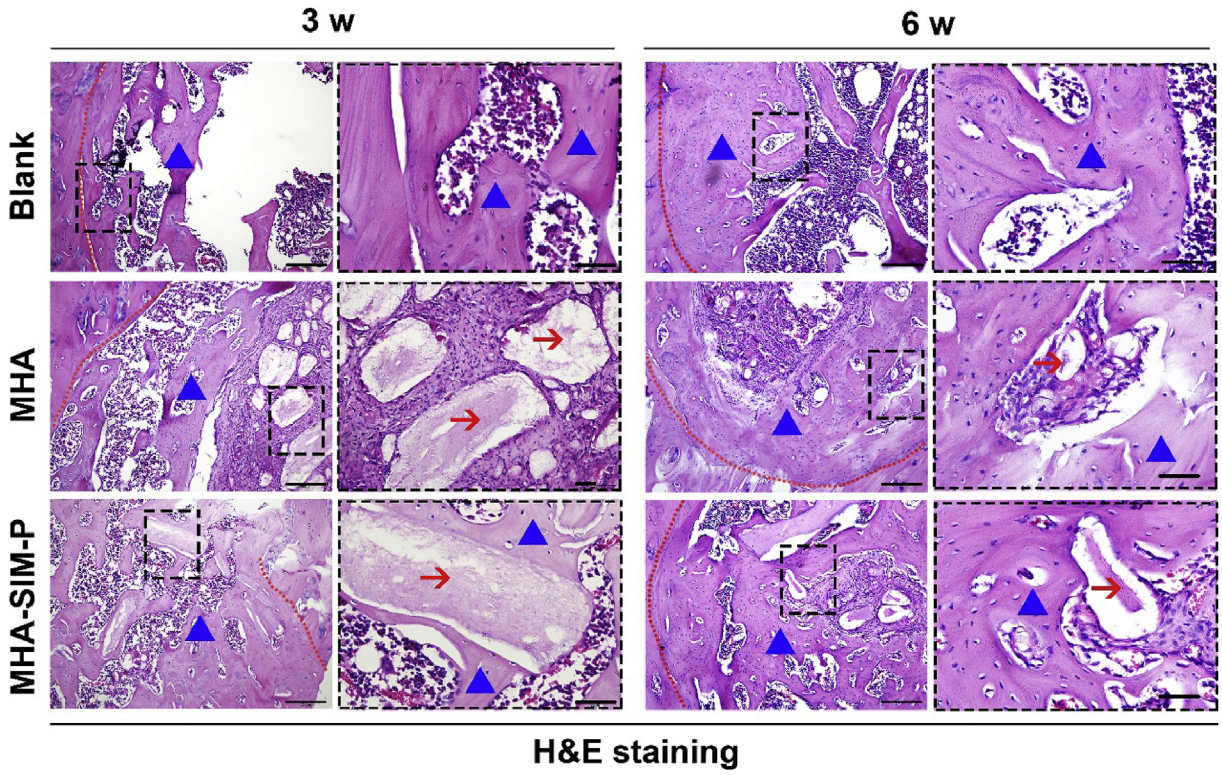

Fig. 4. H&E staining of new bone matrix deposition within defects among the Blank, MHA, and MHA-SIM-P groups in OVX rats after 3 and 6 weeks. Lower magnification (×100; Bar = 200 μm); Higher magnification (×400; Bar = 50 μm). (The blue triangle indicates the new bone, and the red arrow indicates the material remnants.).

compared to the other three groups. In addition, no statistical differences were observed between MHA and MHA-SIM-P group because the remaining MHA and MHA-SIM-P nanoparticles in the bone defects are radiopaque, which might influence the observation of new bone. Even so, the newly formed bone tissue in the MHA-SIM-P group still showed slight increase (p (BV/TV at 3 w) = 0.3688; p (BV/TV at 6 w) = 0.1542; p (Tb. N at 3 w) = 0.3362; p (Tb. N at 6 w) = 0.6158; p (Tb. Sp at 3 w) = 0.0731; p (Tb. Sp at 6 w) = 0.5914).

3.5. Histological and immunohistochemical analysis

3.5.1. Histological assessment

In the Blank control group, sparse new self-healing bone was noticed at the periphery of the defect sites at 3 weeks, with an obvious boundary of native bone (Fig. 4). In the MHA group, the newly generated immature bone was moderately intermingled with connective tissue, embedding the nanoparticles in the central of the defect. Conversely, sections of the MHA-SIM-P group displayed abundant well-arranged bone tissue in the defect, and MHA-SIM-P nanoparticles had filled the newly generated bone tissue 3 weeks following the operation. As study continued, a substantial amount of new bone continued to grow, forming lamellar bone in MHA-SIM-P by 6 weeks leaving no boundary between native and new bone tissue, and nanoparticles which had degraded into small fragments. For both the MHA and Blank groups, newly immature bone tended to mature, but some non-calcified tissue still existed at the medullary of the defects at 6 weeks. Newly generated bone in the Blank group was inferior to that in other groups, both at 3- and 6-weeks post-operation.

TRAP staining was assessed to investigate the capability of osteoclastic resorption (Fig. 5). The number of osteoclasts in the Blank group was statistically higher than in the other groups at either 3 weeks or 6 weeks following the operation. At 3 weeks, mature osteoclasts (stained by TRAP) showed no difference between these two groups. At 6 weeks, osteoclasts took on a shuttle-like shape and lined the trabecular surface, demonstrating an activated bone remodelling process. Meanwhile, an increased number of osteoclasts were found in MHA compared to MHA-SIM-P.

3.5.2. Immunohistochemical assessment

Immunohistochemical indicators, such as OPN and BSP, were stained to observe the mineral deposition and maturation of active bone-formation (Fig. 6). Noticeably, the staining of OPN in the MHA-SIM-P group was more intense and covered a greater area than in the MHA group, and the positive staining area in the Blank group was the least intense and expansive at both 3 and 6 weeks (Fig. 6). The positive staining was specifically located around newly-forming bone lacuna and the remnant nanoparticles. In addition, slightly enhanced staining was observed after operation at 3 weeks more than at 6 weeks, indicating that MHA-SIM-P nanoparticles could induce accelerated mineralisation in the initial phase of bone generation.

The staining of BSP protein was strongest in MHA-SIM-P, followed by MHA and the Blank group at 3 and 6 weeks, and the positive staining area was mainly focused around new bone lacuna. Unsurprisingly the intensity of BSP protein was greater at 6 weeks than at 3 weeks (Fig. 7).

4. Discussion

Decreased bone mineral density and increased adipose tissue volume in the bone marrow cavity is the main manifestation of osteoporosis. The equilibrium among osteoclastic, osteogenic, and adipogenic differentiation gets people interested [26].

In this study, we investigated how the sustained release of SIM from MHA-SIM-P influenced the biological response of OVX BMSCs. On account of the thermal-responsive polymer, SIM could be released at a controlled optimal concentration to stimulate bone formation [27]. It is interesting to find that MHA-SIM-P extraction was able to promote

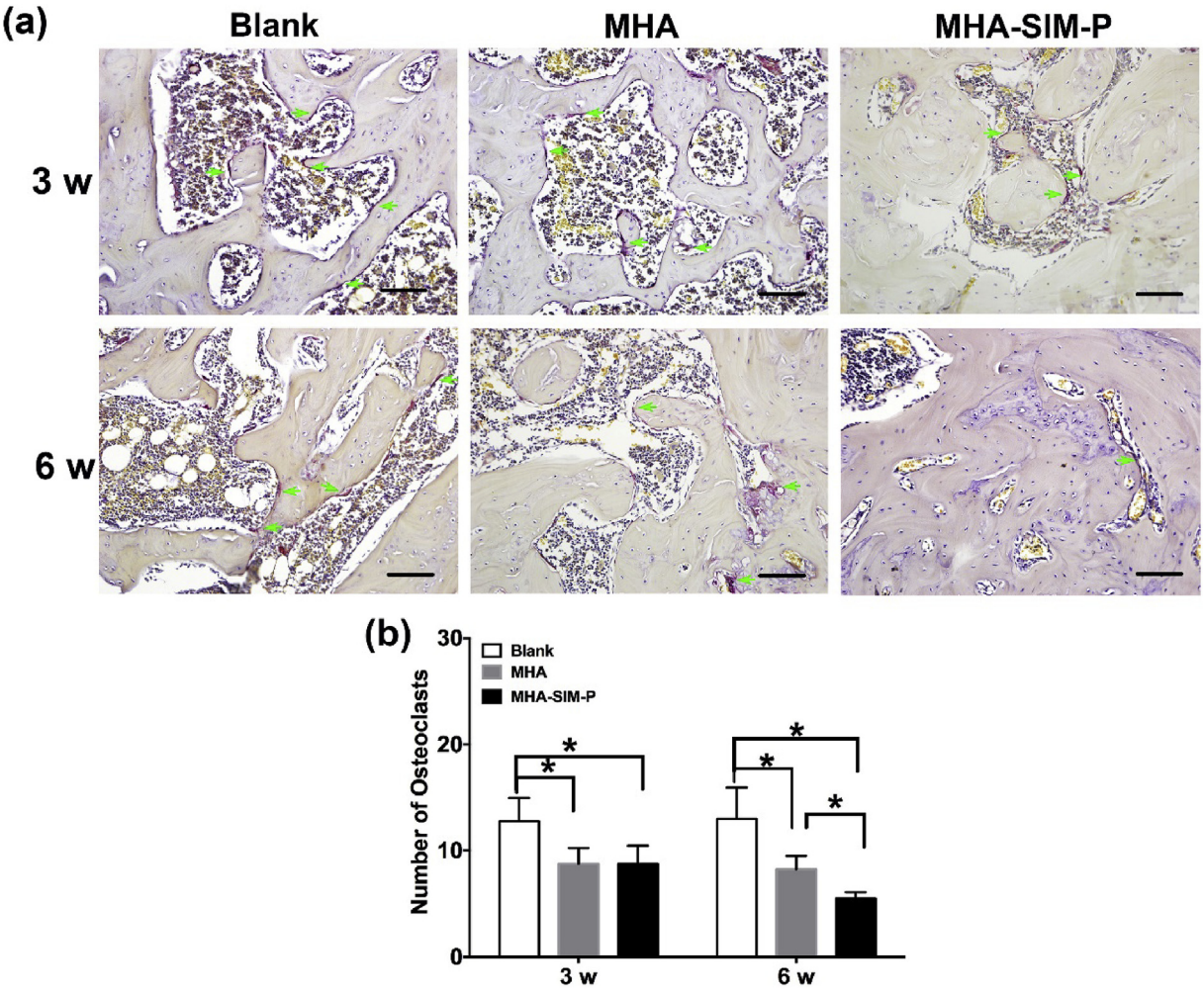

Fig. 5. TRAP staining within defects among Blank, MHA, and MHA-SIM-P groups in OVX rats after 3 and 6 weeks (a). (×200; Bar = 100 μm) The number of TRAP-positive osteoclasts was counted at ×200 magnification (b). n = 3 per group; *p < 0.05. (The green arrow indicates the osteoclasts.).

mineralisation matrix deposition, increase ALP activity after osteogenic induction for 14 days, and upregulate the gene expression of *Runx2* and *OCN* of OVX BMSCs as assessed at 7 and 14 days compared to the Blank or MHA groups. ALP appeared at the early stage of osteoblast differentiation [28]. Since the bioactivity and differentiation ability of OVX MSCs might be damaged in osteoporosis pathology compared with normal MSCs. Thus, the ALP activity in OVX MSCs was not yet improved after osteogenic inducing for 7 days. *Runx2* is the main transcription factor regulating osteogenesis [29], and *OCN* is a significant osteogenic indicator in the later stage of the bone formation process [30,31]. The results confirmed that MHA-SIM-P could increase the osteogenesis ability of OVX BMSCs, implying their therapeutic function *in vitro*.

To prove our hypothesis, MHA-SIM-P nanoparticles were implanted in femur defects in ovariectomised rats to simulate the osteoporotic model. The μCT and H&E staining analysis demonstrated that MHA-SIM-P nanoparticles induce more mineralised tissue than MHA nanoparticles, and more than that of the Blank group. In the condition with osteoporosis, a visible bone resorption can be observed through the smaller osteon diameters [32]. The positive immunohistochemical staining for OPN and BSP was specifically located around newly-forming bone lacuna, and the remnant nanoparticles further proved that MHA-SIM-P's the osteogenic stimulatory effect on OVX BMSCs was companied with the materials degradation. Interestingly, the bone remodelling process occurred with osteoclastic activity. The osteoclasts were relatively high in number following the initial healing period of 3 weeks post-operation, but the number had decreased at 6 weeks, indicating that the bone remodelling was almost complete within the bone defect area (Fig. 5).

The possible MHA-SIM-P mechanisms may be explained as follows: (1) MHA nanoparticles were presented as rod-like shapes at a length of 40–50 nm and a width of 15–20 nm, with well-distributed 4 nm diameter pores inside the nanoparticles, which were a similar structure to the HA of bone tissue. The nanoparticles quickly induced the deposition of HA crystal on the interface under the physiological fluids [33]. (2) Some ions were released from MHA-SIM-P nanoparticles, such as Ca and P ion, becoming the sources of a new bone matrix. Ca ion in concentration of 2–8 mmol was able to promote cell proliferation and activate Ca receptors on the osteoblast to regulate cell differentiation [34,35]. Ten mmol P ion can stimulate the expression of matrix gla protein (MGP) to influence bone formation [36]. Meanwhile, BMP-2 protein can be activated by P ion and promotes the transport of P ions in return [37]. (3) The MHA-SIM-P nanoparticles can promote cell attachment and proliferate due to that the modified hydrophobic poly (N-isopropylacrylamide) brush can improve the adsorption of extracellular matrix protein [38]. (4) A low extracellular pH value did affect bone formation and resorption. Osteoclasts are particularly sensitive to extracellular pH in the range of 7.0–7.2 [39]. The degradation of the materials may change the local microenvironment pH, resulting in less osteoclast activity and more deposition of CaP crystal [40]. (5) SIM was slowly released from the MHA-SIM-P nanoparticle system in therapeutic concentration.

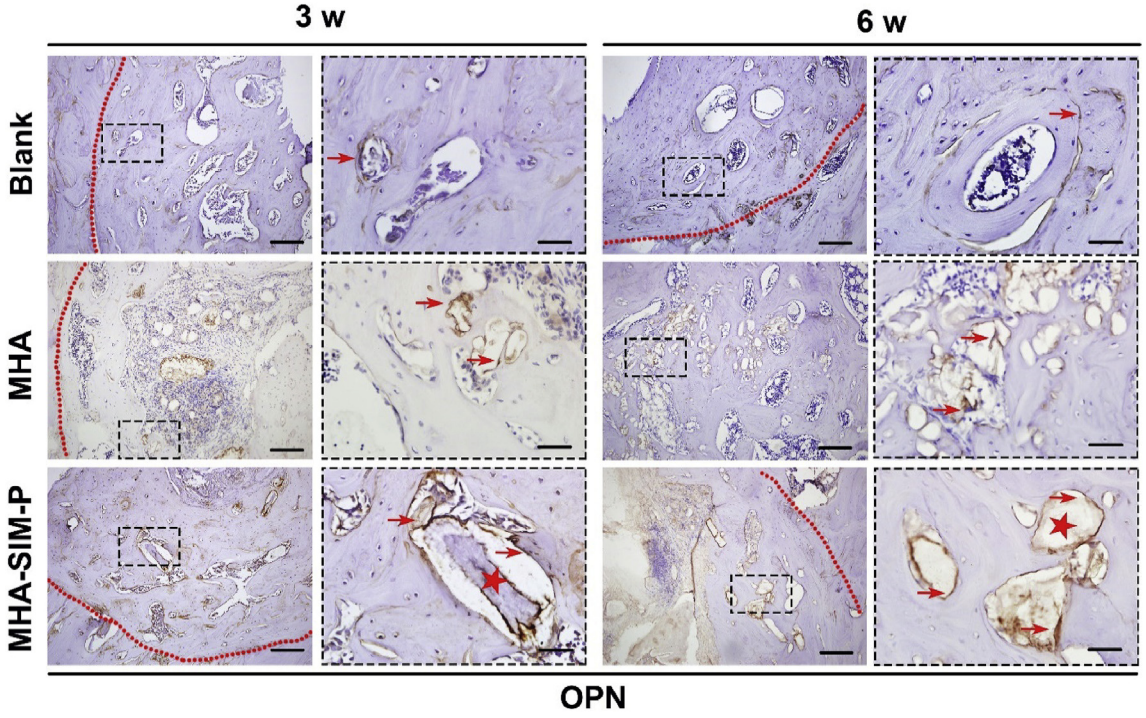

Fig. 6. Immunohistochemical markers of OPN within defects among Blank, MHA, and MHA-SIM-P groups in OVX rats after 3 and 6 weeks. Lower magnification (×100; Bar = 200 μm); Higher magnification (×400; Bar = 50 μm). (The red arrow indicates the brown stained OPN protein, and red star indicates the material remnants.).

Simvastatin was previously administrated as a lipid-lowering drug to treat hyperlipidaemia. SIM was also found benefit to bone regeneration in 1999 [40]. Compared to systemic administration, local delivery of SIM *via* controlled drug delivery systems seems to be more effective and requires a lower dosage. The mechanisms by which SIM acts on bone metabolism were mainly thought to promote osteoblast activity and suppress osteoclastic activity [41]. 1.0×10^{-5} mM to 2.0×10^{-3} mM concentration is able to promote osteogenesis [42,43]. It was reported that drug released from poly (N-isopropylacrylamide) brush-grafted graphene sheets in PBS accumulated to nearly 20% at

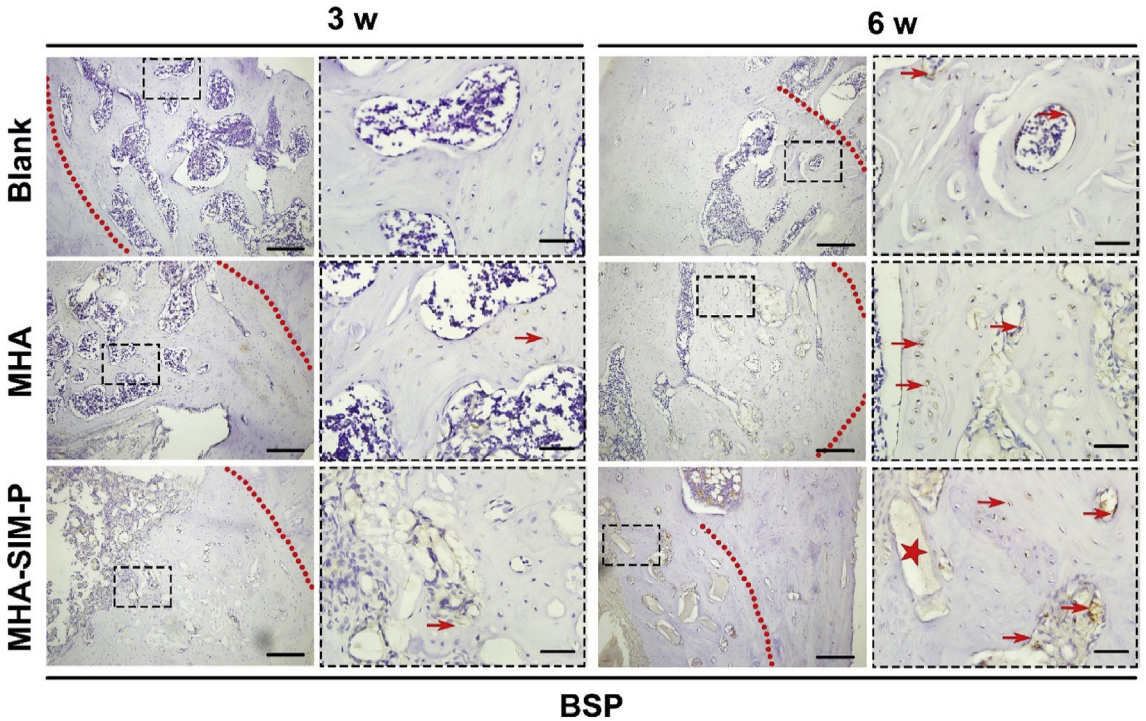

Fig. 7. Immunohistochemical markers of BSP within defects among Blank, MHA, and MHA-SIM-P groups in OVX rats after 3 and 6 weeks. Lower magnification (×100; Bar = 200 μm); Higher magnification (×400; Bar = 50 μm). (The red arrow indicates the brown stained BSP protein, and red star indicates the material remnants.).

37 °C when incubating for 70 h at 37 °C [18]. So, the poly (N-isopropylacrylamide) brush on the surface of MHA can control the slow release of SIM in the local bone defect area to promote new bone formation at physiological temperature. Plenty of cell-signing pathways are involved in the osteogenic, anti-osteoblastic, and anti-adipogenic mechanisms of SIM. It improves osteoblast differentiation by antagonising the TNFα-to-Ras/Rho/MAPK pathway and phosphatidylinositide-3 kinase pathway, as with augmenting BMP-Smad signalling [20]. SIM activates Wnt/β-cantenin signaling [44] to promote osteogenesis, and stimulates VEGF expression in osteoblasts, which is a potentially significant factor in the differentiation of BMSCs towards osteoblasts rather than adipocytes [45,46]. Furthermore, SIM is able to protect osteoblasts from apoptosis *via* the TGF/Smad3 signalling pathway to increase ALP activity, and the mevalonate pathway to reduce the prenylation of GTP-binding protein, blocking osteoblast apoptosis [41,47]. Moreover, it takes part in disturbing osteoclastic activity [48]. SIM promotes the secretion of OPG to compete with RANKL to block osteoclast maturation [49]. Due to the triple balancing effect on osteogenesis, osteoclastic activity, and adipogenic activity, SIM represents a viable treatment for the repair of bone defects in osteoporosis.

5. Conclusion

In conclusion, the sustained release of hydrophobic SIM from polymer brush modified MHA nanoparticles demonstrated an excellent performance in osteogenic differentiation of OVX BMSCs *in vitro* and in the accelerated mineralisation process. Importantly, this SIM delivery system improved bone formation and less osteoclastic response in OVX rats. The positive osteogenic enhancing ability of our nanoparticles suggests the potential therapeutic efficacy of MHA-SIM-P for the repair of osteoporotic local defects.

CRediT authorship contribution statement

Tao Wu: Conceptualization, Methodology, Data curation, Writing - original draft. **Jing Sun:** Conceptualization, Methodology, Writing - original draft. **Lei Tan:** Data curation, Writing - original draft. **Qi Yan:** Data curation. **Lei Li:** Formal analysis, Investigation. **Liangwen Chen:** Software, Visualization. **Xiangmei Liu:** Supervision, Writing - review & editing. **Shi Bin:** Writing - review & editing, Project administration.

Declaration of competing interest

The authors declare that they do not have any financial relation with the commercial identities or associative interests that represents a conflict of interest in connection with the work submitted.

Acknowledgements

The authors declare no conflict of interest for this study. This project was supported by National Natural Science Foundation of China (Grant 81600906), and the Fundamental Research Funds for the Central University of China (No. 2042018kf0108).

References

[1] G.A. Rodan, T.J. Martin, Therapeutic approaches to bone diseases, Science 289 (2000) 1508–1514.
[2] J. Li, A. Ayoub, Y. Xiu, X. Yin, J.O. Sanders, A. Mesfin, L. Xing, Z. Yao, B.F. Boyce, TGFβ-induced degradation of TRAF3 in mesenchymal progenitor cells causes age-related osteoporosis, Nat. Commun. 10 (2019) 2795.
[3] P. Mora-Raimundo, D. Lozano, M. Manzano, M. Vallet-Regi, Nanoparticles to knockdown osteoporosis-related gene and promote osteogenic marker expression for osteoporosis treatment, ACS Nano 13 (2019) 5451–5464.
[4] J. van de Peppel, T. Strini, J. Tilburg, H. Westerhoff, A.J. van Wijnen, J.P. van Leeuwen, Identification of three early phases of cell-fate determination during osteogenic and adipogenic differentiation by transcription factor dynamics, Stem Cell Rep. 8 (2017) 947–960.
[5] E. Shane, Improving fracture risk assessment in older adults, Lancet Diabetes Endocrinol. 7 (2019) 5–7.
[6] D.M. Black, C.G. Solomon, C.J. Rosen, Postmenopausal osteoporosis, N. Engl. J. Med. 374 (2016) 254–262.
[7] L. Wei, J. Ke, I. Prasadam, R.J. Miron, S. Lin, Y. Xiao, J. Chang, C. Wu, Y. Zhang, A comparative study of Sr-incorporated mesoporous bioactive glass scaffolds for regeneration of osteopenic bone defects, Osteoporos. Int. 25 (2014) 2089–2096.
[8] M. Leonida, P. Ispas-Szabo, M. Alexandru Mateescu, Self-stabilized chitosan and its complexes with carboxymethyl starch as excipients in drug delivery, Bioact. Mater. 3 (2018) 334–340.
[9] L. Ma, X. Feng, H. Liang, K. Wang, Y. Song, L. Tan, B. Wang, R. Luo, Z. Liao, G. Li, X. Liu, S. Wu, C. Yang, A novel photothermally controlled multifunctional scaffold for clinical treatment of osteosarcoma and tissue regeneration, Mater. Today (2020), https://doi.org/10.1016/j.mattod.2019.12.005.
[10] M. Li, P. Xiong, F. Yan, S. Li, C. Ren, Z. Yin, A. Li, H. Li, X. Ji, Y. Zheng, Y. Cheng, An overview of graphene-based hydroxyapatite composites for orthopedic applications, Bioact. Mater. 3 (2018) 1–18.
[11] B. Nayak, A. Samant, P.K. Misra, M. Saxena, Nanocrystalline hydroxyapatite: a potent material for adsorption, biological and catalytic studies, Mater. Today: Proc. 9 (2019) 689–698.
[12] B.A.J. Al-Bakhsh, F. Shafiei, A. Hashemian, K. Shekofteh, B. Bolhari, M. Behroozibakhsh, *In-vitro* bioactivity evaluation and physical properties of an epoxy-based dental sealer reinforced with synthesized fluorine-substituted hydroxyapatite, hydroxyapatite and bioactive glass nanofillers, Bioact. Mater. 4 (2019) 322–333.
[13] K. Zhou, P. Yu, X. Shi, T. Ling, W. Zeng, A. Chen, W. Yang, Z. Zhou, Hierarchically porous hydroxyapatite hybrid scaffold incorporated with reduced graphene oxide for rapid bone ingrowth and repair, ACS Nano 13 (2019) 9595–9606.
[14] Y. Cui, H. Dong, X. Cai, D. Wang, Y. Li, Mesoporous silica nanoparticles capped with disulfide-linked PEG gatekeepers for glutathione-mediated controlled release, ACS Appl. Mater. Interfaces 4 (2012) 3177–3183.
[15] L. Li, X. Shi, Z. Wang, M. Guo, Y. Wang, Z. Jiao, P. Zhang, Porous scaffolds of poly (lactic-co-glycolic acid) and mesoporous hydroxyapatite surface modified by poly (γ-benzyl-l-glutamate) (PBLG) for in vivo bone repair, ACS Biomater. Sci. Eng. 5 (2019) 2466–2481.
[16] Z. Ajdukovic, S. Najman, L. Dordevic, V. Savic, D. Mihailovic, D. Petrovic, N. Ignjatovic, D. Uskokovic, Repair of bone tissue affected by osteoporosis with hydroxyapatite-poly-L-lactide (HAp-PLLA) with and without blood plasma, J. Biomater. Appl. 20 (2005) 179–190.
[17] W. Jiang, D. Rutherford, T. Vuong, H. Liu, Nanomaterials for treating cardiovascular diseases: a review, Bioact. Mater. 2 (2017) 185–198.
[18] Y. Pan, H. Bao, N.G. Sahoo, T. Wu, L. Li, Water-Soluble Poly(N-isopropylacrylamide)-graphene sheets synthesized via click chemistry for drug delivery, Adv. Funct. Mater. 21 (2011) 2754–2763.
[19] N. Sameh, U.F. Aly, H.A. Abou-Taleb, A.A.H. Abdellatif, Prospective role of simvastatin on wound healing: review of the literature, J. Bioequivalence Bioavailab. 10 (2018) 36–42.
[20] N. Venkatesan, A.D.T. Liyanage, J. Castro-Nunez, T. Asafo-Adjei, L.L. Cunningham, T.D. Dziubla, D.A. Puleo, Biodegradable polymerized simvastatin stimulates bone formation, Acta Biomater. 93 (2019) 192–199.
[21] T. Maeda, T. Kawane, N. Horiuchi, Statins augment vascular endothelial growth factor expression in osteoblastic cells via inhibition of protein prenylation, Endocrinology 144 (2003) 681–692.
[22] E.G. Long, M. Buluk, M.B. Gallagher, J.M. Schneider, J.L. Brown, Human mesenchymal stem cell morphology, migration, and differentiation on micro and nano-textured titanium, Bioact. Mater. 4 (2019) 249–255.
[23] J.M. Zhang, Y.H. Sun, Y. Zhao, Y.L. Liu, X.H. Yao, B. Tang, R.Q. Hang, Antibacterial ability and cytocompatibility of Cu-incorporated Ni–Ti–O nanopores on NiTi alloy, Rare Met. 38 (2019) 552–560.
[24] J.W. Ma, R. Zan, W.Z. Chen, J.H. Ni, X.N. Zhang, Cell behaviors on surface of pure tantalum with nano-dimpled structure, Rare Met. 38 (2019) 543–551.
[25] W. Amer, K. Abdelouahdi, H.R. Ramananarivo, M. Zahouily, A. Fihri, K. Djessas, K. Zahouily, R.S. Varma, A. Solhy, Microwave-assisted synthesis of mesoporous nano-hydroxyapatite using surfactant templates, CrystEngComm 16 (2014) 543–549.
[26] C. Alexandre, L. Vico, Pathophysiology of bone loss in disuse osteoporosis, Joint Bone Spine 78 (2011) 572–576.
[27] T. Wu, L. Tan, N. Cheng, Q. Yan, Y.F. Zhang, C.J. Liu, B. Shi, PNIPAAM modified mesoporous hydroxyapatite for sustained osteogenic drug release and promoting cell attachment, Mater. Sci. Eng. C 62 (2016) 888–896.
[28] B. Gharibi, A.A. Abraham, J. Ham, B.A. Evans, Adenosine receptor subtype expression and activation influence the differentiation of mesenchymal stem cells to osteoblasts and adipocytes, J. Bone Miner. Res. 26 (2011) 2112–2124.
[29] T. Wu, N. Cheng, C. Xu, W. Sun, C. Yu, B. Shi, The effect of mesoporous bioglass on osteogenesis and adipogenesis of osteoporotic BMSCs, J. Biomed. Mater. Res. 104 (2016) 3004–3014.
[30] Y. Zhang, L. Wei, J. Chang, R.J. Miron, B. Shi, S. Yi, C. Wu, Strontium-incorporated mesoporous bioactive glass scaffolds stimulating in vitro proliferation and differentiation of bone marrow stromal cells and in vivo regeneration of osteoporotic bone defects, J. Mater. Chem. B 1 (2013) 5711–5722.
[31] J. Fu, X. Liu, L. Tan, Z. Cui, Y. Zheng, Y. Liang, Z. Li, S. Zhu, K.W.K. Yeung, X. Feng, X. Wang, S. Wu, Photoelectric-responsive extracellular matrix for bone engineering, ACS Nano 13 (2019) 13581–13594.
[32] P. Milovanovic, E.A. Zimmermann, C. Riedel, A.V. Scheidt, L. Herzog, M. Krause, D. Djonic, M. Djuric, K. Püschel, M. Amling, R.O. Ritchie, B. Busse, Multi-level characterization of human femoral cortices and their underlying osteocyte network

reveal trends in quality of young, aged, osteoporotic and antiresorptive-treated bone, Biomaterials 45 (2015) 46–55.
[33] W. Wang, K.W.K. Yeung, Bone grafts and biomaterials substitutes for bone defect repair: a review, Bioact. Mater. 2 (2017) 224–247.
[34] A. Lode, C. Heiss, G. Knapp, J. Thomas, B. Nies, M. Gelinsky, M. Schumacher, Strontium-modified premixed calcium phosphate cements for the therapy of osteoporotic bone defects, Acta Biomater. 65 (2018) 475–485.
[35] P.J. Marie, The calcium-sensing receptor in bone cells: a potential therapeutic target in osteoporosis, Bone 46 (2010) 571–576.
[36] S. Khoshniat, A. Bourgine, M. Julien, M. Petit, P. Pilet, T. Rouillon, M. Masson, M. Gatius, P. Weiss, J. Guicheux, L. Beck, Phosphate-dependent stimulation of MGP and OPN expression in osteoblasts via the ERK1/2 pathway is modulated by calcium, Bone 48 (2011) 894–902.
[37] A. Suzuki, C. Ghayor, J. Guicheux, D. Magne, S. Quillard, A. Kakita, Y. Ono, Y. Miura, Y. Oiso, M. Itoh, J. Caverzasio, Enhanced expression of the inorganic phosphate transporter Pit-1 is involved in BMP-2-induced matrix mineralization in osteoblast-like cells, J. Bone Miner. Res. 21 (2006) 674–683.
[38] Q. Yu, L.M. Johnson, G.P. López, Nanopatterned polymer brushes for triggered detachment of anchorage-dependent cells, Adv. Funct. Mater. 24 (2014) 3751–3759.
[39] T.R. Arnett, Extracellular pH regulates bone cell function, J. Nutr. 138 (2008) 415s–418s.
[40] W. Liu, X. Dan, W.W. Lu, X. Zhao, C. Ruan, T. Wang, X. Cui, X. Zhai, Y. Ma, D. Wang, W. Huang, H. Pan, Spatial distribution of biomaterial microenvironment pH and its modulatory effect on osteoclasts at the early stage of bone defect regeneration, ACS Appl. Mater. Interfaces 11 (2019) 9557–9572.
[41] A. Moshiri, A.M. Sharifi, A. Oryan, Role of simvastatin on fracture healing and osteoporosis: a systematic review on in vivo investigations, Clin. Exp. Pharmacol. Physiol. 43 (2016) 659–684.
[42] X. Liu, X. Li, L. Zhou, S. Li, J. Sun, Z. Wang, Y. Gao, Y. Jiang, H. Lu, Q. Wang, J. Dai, Effects of simvastatin-loaded polymeric micelles on human osteoblast-like MG-63 cells, Colloids Surf., B 102 (2013) 420–427.
[43] A. Oryan, A. Kamali, A. Moshiri, Potential mechanisms and applications of statins on osteogenesis: current modalities, conflicts and future directions, J. Contr. Release 215 (2015) 12–24.
[44] L.J. Qiao, K.L. Kang, J.S. Heo, Simvastatin promotes osteogenic differentiation of mouse embryonic stem cells via canonical Wnt/β-catenin signaling, Mol. Cell 32 (2011) 437–444.
[45] E.R. Balmayor, Targeted delivery as key for the success of small osteoinductive molecules, Adv. Drug Deliv. Rev. 94 (2015) 13–27.
[46] Y. Liu, A.D. Berendsen, S. Jia, S. Lotinun, R. Baron, N. Ferrara, B.R. Olsen, Intracellular VEGF regulates the balance between osteoblast and adipocyte differentiation, J. Clin. Invest. 122 (2012) 3101–3113.
[47] C.J. Edwards, T.D. Spector, Statins as modulators of bone formation, Arthritis Res. 4 (2002) 151–153.
[48] B.F. Boyce, L. Xing, G. Franzoso, U. Siebenlist, Required and nonessential functions of nuclear factor-kappa B in bone cells, Bone 25 (1999) 137–139.
[49] D.G. Soares, Z. Zhang, F. Mohamed, T.W. Eyster, C.A. de Souza Costa, P.X. Ma, Simvastatin and nanofibrous poly(l-lactic acid) scaffolds to promote the odontogenic potential of dental pulp cells in an inflammatory environment, Acta Biomater. 68 (2018) 190–203.